Journal of Materials Chemistry A

# Ultrafast Cathode Characteristics of a Nano-$V_2(PO_4)_3$ Carbon Composite for Rechargeable Magnesium Batteries

| | |
|---|---|
| Journal: | *Journal of Materials Chemistry A* |
| Manuscript ID | TA-ART-09-2023-005912.R1 |
| Article Type: | Paper |
| Date Submitted by the Author: | 04-Dec-2023 |
| Complete List of Authors: | Harada, Yuta; Tokyo University of Agriculture and Technology, Department of Applied Chemistry<br>Chikaoka, Yu; Tokyo University of Agriculture and Technology, Department of Applied Chemistry<br>Kasai, Marina; Tokyo University of Agriculture and Technology, Department of Applied Chemistry<br>Koizumi, Kyoya; Tokyo University of Agriculture and Technology, Department of Applied Chemistry<br>Iwama, Etsuro; Tokyo University of Agriculture & Technology, Department of Applied Chemistry<br>Okita, Naohisa; Tokyo University of Agriculture and Technology, Department of Applied Chemistry<br>Orikasa, Yuki; Ritsumeikan University, Department of Applied Chemistry<br>Naoi, Wako; K & W Inc.,<br>Naoi, Katsuhiko; Tokyo University of Agriculture and Technology, Department of Applied Chemistry |
| | |

ARTICLE

# Ultrafast Cathode Characteristics of a Nano-$V_2(PO_4)_3$ Carbon Composite for Rechargeable Magnesium Batteries

Received 00th January 20xx,
Accepted 00th January 20xx

DOI: 10.1039/x0xx00000x

Yuta Harada[a], Yu Chikaoka *[ab], Marina Kasai[a], Kyoya Koizumi[a] , Etsuro Iwama [ab], Naohisa Okita[a], Yuki Orikasa[c], Wako Naoi[d], and Katsuhiko Naoi *[abe]

Magnesium rechargeable batteries (Mg batteries) are currently attracting attention as high-energy and low-cost energy storage devices that can replace lithium-ion batteries. Within this context, $V_2(PO_4)_3$ is a promising material for high-voltage and high-rate cathodes for Mg batteries. However, the strong electrostatic attraction between $Mg^{2+}$–anion degrades the $Mg^{2+}$ diffusion in the solid-state of the cathode, which hindered the room-temperature operation. Further, the detailed charge–discharge mechanism of $V_2(PO_4)_3$ during $Mg^{2+}$ insertion/extraction is not yet fully understood. Here, we synthesized $V_2(PO_4)_3$ nanocrystals (50 nm), which are highly dispersed and directly embedded in conductive carbon, for realizing ultrafast cathode reaction for Mg batteries. The $V_2(PO_4)_3$/carbon composite exhibited a high capacity of 210 mAh $g^{-1}$ (at 1C-rate) and 110 mAh $g^{-1}$ (at 10C-rate, i.e., under ultrafast conditions) during $Mg^{2+}$ insertion/extraction even at room temperature. The phase transition and valence change of vanadium in $Mg_xV_2(PO_4)_3$ were evaluated by *in-situ* X-ray diffraction (XRD) and X-ray absorption fine structure (XAFS) analyses. Both *in-situ* measurements revealed that $Mg^{2+}$ insertion/extraction of $Mg_xV_2(PO_4)_3$ ($0.5 \le x \le 1.3$) proceeds reversibly with a valence change of vanadium through a solid-solution reaction, unlike the $Li^+$ insertion/extraction of $Li_xV_2(PO_4)_3$ ($1 \le x \le 3$) via a two-phase reaction. Our findings provide a promising synthesis method of $V_2(PO_4)_3$ for ultrafast and high-voltage cathodes for practical Mg batteries and experimental evidence for a unique charge–discharge mechanism in $Mg_xV_2(PO_4)_3$.

## Introduction

The demand for energy storage systems (ESSs) such as lithium-ion batteries (LIBs) for power supply applications, e.g., smart grid systems and electric vehicles, has been increasing exponentially [1]. In this context, to meet the market demand for large-scale energy systems, post-LIBs without using rare metals (Li, Co, Mn) are required to ensure sustainability in the supply of battery materials [2]. Among these post-LIBs, Magnesium rechargeable batteries (Mg batteries), in which $Mg^{2+}$ serves as the carrier ion, are considered promising ESSs. Mg batteries offer several advantages over LIBs; the high volumetric energy density of the metal anode (Mg: 3833 and Li: 2046 mAh $cm^{-3}$), low redox potential (Mg: −2.37 V and Li: −3.04 V *vs.* SHE) [2–5], natural abundance of Mg resources (~2% of the Earth's crust) [6], and high safety derived from the less-dendritic effect compared to Li metal [7–9]. In previous studies of Mg batteries, on the anode side, considerable effort has been devoted for realizing reversible $Mg^{2+}$ dissolution and deposition in terms of Mg alloys, electrolytes, and artificial interfaces [3,10–12]. Focusing on the cathode side, many technical difficulties have yet to be overcome toward designing high-power and high-energy Mg batteries. Specifically, the electrostatic interaction of $Mg^{2+}$ is greater than that of monovalent ions, resulting in slower $Mg^{2+}$ mobility through the cathode and a low-rate reaction [13]. This slow reaction requires high temperatures and/or long-time charge–discharge operations. For example, chalcogenides with Chevrel phases ($Mo_6S_8$), other chalcogenides ($WSe_2$, layered $TiSe_2$, spinel $Ti_2S_4$), and oxides ($V_2O_5$, $MnO_2$) cathodes required lengthy charge–discharge processes (10–60 h) and high-temperature operation (100°C) [8,14–20]. In addition, these Mg cathodes have a low operating voltage range (1.0–2.0 V *vs.* $Mg/Mg^{2+}$) [8,14–20], which lowers the energy density of Mg batteries.

To overcome these problems, the researchers recently focused on developing Mg cathodes with high $Mg^{2+}$ mobility and high operating voltages. For example, spinel oxides ($MgMn_2O_4$)[21–23] and polyanion compounds ($FePO_4$, $V_2(PO_4)_3$) [24–28] have been reported. Among them, polyanion compounds, which are widely used as cathode materials for LIBs [29–33], are promising Mg cathodes because of their high reaction potential and high thermal stability. These favorable properties are derived from the inductive effect of the strong covalent bonding of the $PO_4$ unit [34–36]. For instance, during $Mg^{2+}$

[a] Department of Applied Chemistry, Tokyo University of Agriculture & Technology, 2-24-16 Naka-cho, Koganei, Tokyo 184-8558, Japan. Email: chika@go.tuat.ac.jp; k-naoi@cc.tuat.ac.jp
[b] Global Innovation Research Organization, Tokyo University of Agriculture & Technology, 2-24-16 Naka-cho, Koganei, Tokyo, 184-8588, Japan
[c] Department of Applied Chemistry, Ritsumeikan University, 1-1-1 Nojihigashi, Kusatsu 525-8577, Japan
[d] Division of Art and Innovative Technologies, K & W Inc., 1-3-16-901 Higashi, Kunitachi, Tokyo 186-0002, Japan
[e] Advanced Capacitor Research Center, Tokyo University of Agriculture & Technology, 2-24-16 Naka-cho, Koganei, Tokyo 184-8558, Japan
† Electronic Supplementary Information (ESI) available:
See DOI: 10.1039/x0xx00000x

insertion/extraction, the $FePO_4$ cathode had a higher redox potential of 2.0–2.5 V *vs.* $Mg/Mg^{2+}$ [26–28]. Further, the defective $FePO_4$ nanoparticles embedded in conductive carbon exhibited a high capacity of 170 mAh $g^{-1}$ at 1/20C-rate even at room temperature. In a recent study, the use of the dual-salt electrolyte [magnesium bis(trifluoromethanesulfonyl)amide ($Mg(TFSA)_2$) + spiro-(1,1')-bipyrolidinium tetrafluoroborate ($SBPBF_4$)] enhanced the rate capabilities of $FePO_4$ to realize a high capacity of more than 150 mAh $g^{-1}$ at 0.5C-rate at room temperature [37].

The monoclinic $V_2(PO_4)_3$ framework, which is prepared by the complete delithiation of the monoclinic lithium vanadium phosphate ($Li_3V_2(PO_4)_3$, LVP) used as the LIBs cathode [29,36], is another promising Mg cathode with a high voltage and high rate. Indeed, in $Mg^{2+}$ insertion/extraction, the redox potential of the $V_2(PO_4)_3$ cathode has been estimated to be as high as 3.3 V *vs.* $Mg/Mg^{2+}$ by DFT calculations [38]. Further, LVP has a high $Li^+$ diffusion coefficient ($10^{-8}$–$10^{-9}$ $cm^2$ $s^{-1}$) [39,40] owing to the three-dimensional diffusion pathway of $Li^+$ [41], and therefore, high $Mg^{2+}$ diffusivity would be expected. In fact, DFT calculations indicated that nanosized $V_2(PO_4)_3$ particles (50 nm) enable the charge–discharge with $Mg^{2+}$ diffusion at 1/2C-rate at room temperature [13,38]. However, contrary to expectations, in experiments with $Mg_xV_2(PO_4)_3$, charge–discharge was only realized at the low rate (1/20C-rate) and at a high temperature (50°C) [24]. This low-rate reaction could be attributed to the large particle size (150–400 nm) and lack of optimization of the composite morphology. On the other hand, the co-insertion of $Li^+$ and $Mg^{2+}$ into the $V_2(PO_4)_3$ framework realized a high reversible capacity of 120 mAh $g^{-1}$ at 100 mA $g^{-1}$ (0.76C-rate) at room temperature [42]. This enhancement could be due to the improved $Mg^{2+}$ diffusion in the solid state because of the concerted $Li^+/Mg^{2+}$ insertion, as was also reported for the Chevrel $Mo_6S_8$ in $Li^+/Mg^{2+}$ electrolytes. However, to the best of our knowledge, the charge–discharge rate of $V_2(PO_4)_3$ based on pure $Mg^{2+}$ insertion/extraction has not reached the anticipated level (a rate of approximately 1/2C-rate), as initially predicted by DFT calculations. Focusing on the charge–discharge curve, $Mg_xV_2(PO_4)_3$ exhibits a slope shape, resembling that of a solid-solution reaction. This behavior differs from that of $Li_xV_2(PO_4)_3$ (three plateaus attributed to a two-phase reaction), even at the same potential range (from −1.0 to 1.2 V *vs.* $Ag/Ag^+$) [24]. However, analysis of the charge–discharge mechanisms of $Mg_xV_2(PO_4)_3$ has been limited to intermittent observations of the phase transition, and valence changes of vanadium in $V_2(PO_4)_3$ using *ex-situ* XRD/X-ray absorption fine structure (XAFS) analysis at a few states-of-charge (SOC) [24,42]. A precise understanding of the reaction behavior of $Mg_xV_2(PO_4)_3$ would require *in-situ* XRD and *in-situ* XAFS to be performed at a large number of SOCs.

In this study, we synthesized a nanocrystalline-$V_2(PO_4)_3$/carbon composite via the original synthesis process (ultracentrifugation method) [25,32] for the Mg batteries cathode. Further, by changing the carbon content and species (Ketjen black(KB) or multiwalled carbon nanotubes (MWCNTs)), we aimed to optimize the particle size and morphology of the composite of $V_2(PO_4)_3$ with carbon. The $V_2(PO_4)_3$ composites synthesized with high-KB content (ratios of 5:5 and 4:6) formed nanosized $V_2(PO_4)_3$ particles and demonstrated high power performance with a high capacity exceeding 200 mAh $g^{-1}$ at 1C-rate at room temperature. Furthermore, during charge–discharge of $Mg_xV_2(PO_4)_3$, the changes in the valence of vanadium and the phase transition of $V_2(PO_4)_3$ were evaluated by *in-situ* XRD and *in-situ* XAFS analyses. Both *in-situ* measurements indicated that reversible valence change and phase transition occurred during charge–discharge of $Mg_xV_2(PO_4)_3$. In addition, $Mg_xV_2(PO_4)_3$ reacts via a solid-solution reaction in the potential range in which $Li_xV_2(PO_4)_3$ is known to proceed via a two-phase reaction during charge–discharge. Our study proposes a strategy to guide the synthesis of high-voltage and high-power cathodes for practical application in Mg batteries and provides experimental evidence that $Mg^{2+}$ insertion/extraction occurs by way of a unique charge–discharge mechanism.

## Experimental methods

### Materials

$NH_4VO_2$ (99%, Kanto Chemical Co.), $LiCH_3COO$, and $H_3PO_4$ were used as the sources of V, Li, and $PO_4$, respectively, while citric acid ($C_6H_8O_7$) (99.5%, Sigma-Aldrich) and ethylene glycol (99%, Wako Pure Chemical Industries) were used as chelating agents. Hollow-structured Ketjen black (KB; EC600JD, Ketjen Black International) having 50-nm-diameter primary particles with a specific surface area of 1270 $m^2$ $g^{-1}$ and multiwalled carbon nanotubes (MWCNTs) with a specific surface area of 240 $m^2$ $g^{-1}$ [44] were selected as the precursor carbon matrix for embedding the nanoscale $Li_3V_2(PO_4)_3$. Ultrapure water (17 Ω cm) was used as the medium for the entire preparation scheme.

### Material Synthesis

$Li_3V_2(PO_4)_3$/carbon composites (LVP/KB or LVP/MWCNT) were prepared via a previously reported "ultracentrifugation (UC)" method [37]. Two solutions, A and B, were prepared. $LiCH_3COO$, $NH_4VO_2$, $C_6H_8O_7$, and ethylene glycol in a molar ratio of 3:2:2:8 were dissolved in $H_2O$ (solution A). $H_3PO_4$ solutions and either KB or MWCNTs were mixed for 30 min using ultrasonication and then subjected to UC for 5 min to form a blackish gel (solution B). The addition of solution A to B was followed by second UC for 5 min. After a drying process at 80°C for 12 h under a vacuum, the precursor was annealed for 33 min (heating for 3 min and holding for 30 min) at 800°C under a nitrogen flow to yield the LVP composite powder with various carbon contents (KB: 30 wt%, 40 wt%, 50 wt%, and 60 wt%, and MWCNTs: 50 wt%).

The delithiated-$V_2(PO_4)_3$ for the Mg cathodes was obtained by electrochemically extracting $Li^+$ from the $Li_3V_2(PO_4)_3$ cathodes (LVP/KB or LVP/MWCNT). LVP cathodes were prepared from the composite powder and poly(vinylidene difluoride) (PVdF) binder mixed in a weight ratio of 90:10. For the Li extraction, a laminate cell was assembled using an LVP cathode, Li-metal counter electrode, 1 M lithium hexafluorophosphate ($LiPF_6$)/[ethylene carbonate (EC):diethyl

carbonate (DEC) of 1:1 vol%] as the electrolyte, and a 25-µm-thick polypropylene separator. The constructed laminate cell was then charged under constant-current to 4.8 V *vs*. Li/Li$^+$ at 1C-rate and maintained under constant-voltage conditions at 4.8 V *vs*. Li/Li$^+$ for 3 h (1C-rate = 131.5 mAh g$^{-1}$ of the $Li_3V_2(PO_4)_3$ active material). Subsequently, the cell was disassembled in a dry room (dew point < −40°C), and the delithiated-$V_2(PO_4)_3$ (VP/KB or VP/MWCNT) was rinsed with dimethyl carbonate (DMC) solvent.

**Material Characterization**

X-ray diffraction (XRD, Rigaku SmartLab) analysis was used to characterize the crystalline structure of LVP/KB and LVP/MWCNT. The carbon content in the composites was determined by thermal analysis in a synthetic air atmosphere (20% $O_2$, 80% $N_2$) using a thermogravimetric differential thermal analyzer (TG/DTA, Seiko Instruments TG/DTA6300). The detailed nanostructural features of the composites, such as the LVP particle size and composite morphology with conductive carbons, were characterized by high-resolution transmission electron microscopy (HRTEM, Hitachi H9500 model). The delithiated VP/KB was analyzed by electron energy loss spectroscopy (EELS). $Mg^{2+}$ insertion/extraction into VP/KB was confirmed by scanning transmission electron microscopy combined with energy-dispersive X-ray spectroscopy (STEM-EDX, Hitachi, HD2700).

**Electrochemical Measurement**

Two-electrode laminate cells were assembled using the $Mg^{2+}$-battery configuration with either VP/KB or VP/MWCNT as the cathode, an activated carbon (AC) counter electrode, and 25 µm-thick monolayer polypropylene separator (Celgardµ2400, Celgard) with a dual-salt electrolyte [0.5 M $Mg(TFSA)_2$ + 1 M $SBPBF_4$/dimethyl carbonate (DMC)] [43]. Counter electrodes of AC (YP-50F, Kuraray; thickness, 400 µm; density, 0.41 g cm$^{-3}$) were prepared by mixing AC, KB, and polytetrafluoroethylene (PTFE) as the binder in a weight ratio of 80:10:10. Prior to the electrochemical measurements, the AC electrodes were cut into 2 cm × 2 cm pieces and dried overnight at 200°C under vacuum. The mass loading of the AC counter electrode was ten times higher than that of the $V_2(PO_4)_3$ working electrode to ensure the AC potential remained at a constant value (0.12–0.27 V *vs*. Ag/Ag$^+$) against the $V_2(PO_4)_3$ working electrodes (Fig. S1). In the charge–discharge tests, the voltage range was from −1.2 to 1.3 V *vs*. AC (corresponding to potential range of 1.1–3.6 V *vs*. Mg/$Mg^{2+}$), and different C-rates (1, 2, 5, 10, 20, 50, to 100) were used for every three charge–discharge cycles (1C-rate = 131.5 mAh g$^{-1}$ of the $V_2(PO_4)_3$ active material) (HJ 1001 SD 8, Hokuto). As a reference with which to compare the performance of the $Mg^{2+}$-battery systems, a Li$^+$ electrolyte cell with the same electrode composition as the $Mg^{2+}$-battery was constructed with 1 M $LiPF_6$/EC:DEC as the electrolyte.

***In-situ* XAFS**

*In-situ* XAFS measurements at the V K-edges were performed at the composite samples in transmission mode at the BL01B1 beamline of the synchrotron radiation facility SPring-8 (Hyogo, Japan), as reported previously [25,33]. Laminate cells for *in-situ* XAFS measurements were assembled using a VP/KB cathode, the AC counter electrode with a mass loading ten times higher than that of the cathode and a 35-µm-thick cellulose separator with a dual-salt electrolyte [0.5 M $Mg(TFSA)_2$ + 1 M $SBPBF_4$/DMC]. Charge–discharge tests were performed within a voltage range of −1.3 to 1.3 V *vs*. AC (corresponding to potential range of 1.0–3.6 V *vs*. Mg/$Mg^{2+}$) during the first cycle at 0.5C-rate (1C-rate = 131.5 mAh g$^{-1}$ of the VP active material). Prior to the XAFS measurements, the cell was discharged in constant-current mode to −1.3 V *vs.* AC at 0.5C-rate. The obtained XAFS spectra were analyzed using the spectral fitting software REX2000 (Rigaku Corp.) to evaluate the number of different V species with different oxidation states using $V^{3+}$ ($V_2O_3$) and $V^{4+}$($VO_2$) as the references.

***In-situ* XRD analysis**

*In-situ* XRD analyses were conducted using the *in-situ* XRD cell (Rigaku) [32] consisting of a VP/KB cathode, glass separators (GF/F, Whatman Ltd.), and the AC counter electrode with a mass loading five times higher than that of the cathode. Charge–discharge tests were performed from −1.2 to 1.3 V *vs*. AC (corresponding to 1.1–3.6 V *vs*. Mg/$Mg^{2+}$) during the first cycle at 0.25C-rate (1C-rate = 131.5 mAh g$^{-1}$ of the VP active material). *In-situ* XRD patterns were recorded in the 2$\vartheta$ range of 15–40° at a scan speed of 0.025° s$^{-1}$ using a Smart-lab diffractometer (Rigaku, CuKα radiation ($\lambda$=1.54 Å)) in the Bragg-Brentano configuration.

## Results and discussion

**Characterization of Pristine $Li_3V_2(PO_4)_3$ Carbon Composite Materials**

Fig.1 shows the XRD patterns and TGA of the LVP/KB and LVP/MWCNT composites. In the case of KB as the composite carbon, LVP composites were synthesized with different carbon contents (30 wt%, 40 wt%, 50 wt%, and 60 wt%), which were labeled LVP/KB(7:3), LVP/KB(6:4), LVP/KB(5:5), and LVP/KB(4:6), respectively. Additionally, to assess the effect of MWCNTs as a different composite carbon species, we also synthesized a VP composite with 50 wt% of MWCNTs (LVP/MWCNT (5:5)). In Fig. 1a, the XRD patterns of all the prepared LVP/carbon composites showed the peaks of monoclinic $Li_3V_2(PO_4)_3$ [46] appeared on the broad peak (2$\vartheta$ = 20–30°) of KB or MWCNTs (Fig. S2), and no other peaks derived from impurities were detected. TGA was performed in an atmosphere of synthetic air to determine the residual weight ratio of the composite carbon (Fig. 1b, c). The carbon contents in these composites were estimated from the decrease in weight at approximately 450°C derived from the carbon combustion: 58 wt% (LVP/KB(4:6)), 47 wt% (LVP/KB(5:5)), 41 wt% (LVP/KB(6:4)), 30 wt% (LVP/KB(7:3)), and 50 wt% (LVP/MWCNT(5:5)), indicating that the carbon content in the

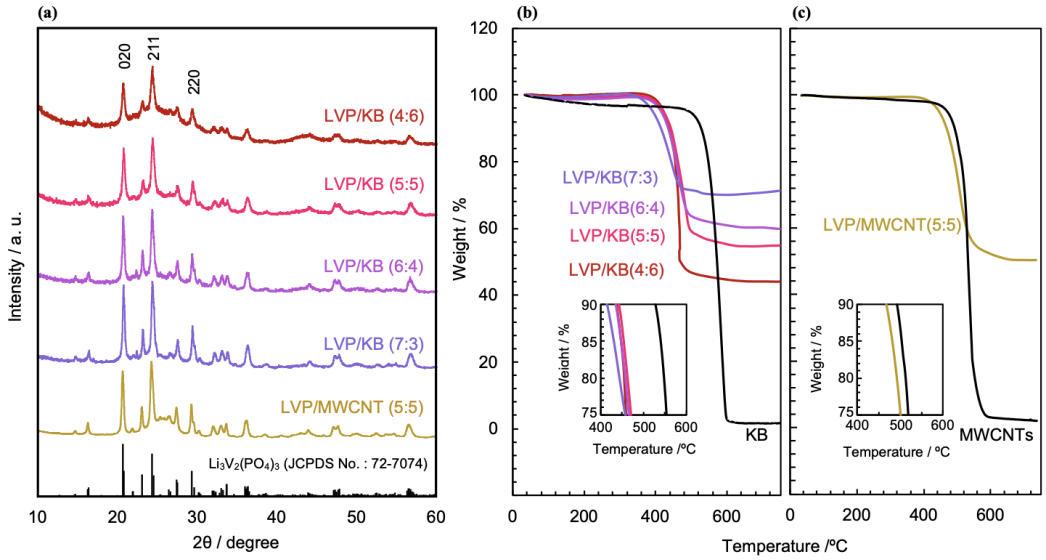


**Figure 1.** (a) XRD patterns of the LVP/KB and LVP/MWCNT composites sintered at different carbon contents of 30 wt%, 40 wt%, 50 wt%, and 60 wt%. All composites showed three major peaks attributed to the (020), (211), and (220) reflections of the LVP crystal (JCPDS No. 72-7074). (b, c) TGA thermograms of the (b) LVP/KB composites and KB, and (c) LVP/MWCNT composite and MWCNTs. The measurements were performed at a sweep rate of 5°C $min^{-1}$ from ambient temperature to 750°C under a synthetic air atmosphere. Enlarged views of the temperature range in which carbon combustion occurred are shown in the insets of (b) and (c).

composite was approximately the same as the preparation ratio of all the composites. Judging from the combined XRD and TGA results, all samples were successfully synthesized as high-purity LVP/carbon composites with the designed carbon contents. The combustion temperatures of LVP/carbon composites were lower than those of the corresponding carbon(KB or MWCNTs) : approximately 100°C lower for the KB composites and approximately 20°C lower for the MWCNTs composites (insets in Fig. 1b,c). These decreases suggest that direct bonding occurred between the dangling bonds of the LVP crystal and the functional groups on the carbon surface, as reported previously [32]. LVP/KB(7:3), which has the lowest weight ratio of carbon, had the lowest combustion temperature (430°C) (inset in Fig. 1b). This observation also highlights the impact of direct bonding on the combustion temperature of KB. Specifically, the ratio of KB directly bonded with LVP to KB without such bonding appears to be the largest in LVP/KB (7:3) among tested LVP/KB composites. Interestingly, the combustion temperature of LVP/MWCNT(5:5) (500°C) (inset in Fig. 1c) was higher than that of LVP/KB(5:5) with the same carbon content, despite the similar combustion temperatures of pristine KB and MWCNT (580-600˚C). This discrepancy suggests that the amount of bonded carbon (MWCNT) in LVP/MWCNT is lower than in LVP/KB. Several factors could contribute to this observation, including the fact that MWCNT possesses fewer functional groups and smaller surface area of MWCNTs (240 $m^2$ $g^{-1}$) compared to that of KB (1270 $m^2$ $g^{-1}$), which results in less contact area between LVP and MWCNT.

The relationship between carbon contents/species and crystal growth was investigated by the apparent average crystallite size of LVP, which was calculated by converting the full width at half maximum (FWHM) values obtained from the XRD pattern of LVP (020) based on Scherrer equation [29]. The calculated crystallite sizes increased in the following order (Table S1): LVP/KB(5:5)(29 nm) < LVP/KB(4:6)(30 nm) < LVP/MWCNT(5:5)(37 nm) < LVP/KB(6:4) = LVP/KB(7:3)(39 nm). The KB-based composites with carbon contents of 50 wt% or higher (LVP/KB(5:5) and LVP/KB(4:6)) had smaller crystallites than those with carbon contents less than 50 wt% (LVP/KB(6:4) and LVP/KB(7:3)). This trend could originate from the process of crystal growth in the UC method. In the UC method, the ion sources of the LVP crystal ($V^{5+}$, $Li^{+}$, $PO_4^{3-}$) are coordinated to the functional groups on the conductive carbon surfaces and chelating agent. Then, these ions form LVP crystals with the neighboring ions during the annealing process [37]. The high-KB content systems (LVP/KB(5:5) and LVP/KB(4:6)) may exhibit a broader ion distribution due to the abundance of functional groups on the carbon material. In turn, this lead to a lower collision rate between neighboring ion sources, which suppresses excessive crystal growth and decreases the crystallite size. On the other hand, the MWCNTs composite (LVP/MWCNT(5:5), 39 nm) had larger crystallites than the KB composite (LVP/KB(5:5), 29 nm), even for the same carbon content, suggesting that excessive crystal growth occurred. As indicated by the TGA results, the MWCNTs have fewer functional groups on the surface of the carbon that can bind to ions, resulting in a narrower ion distribution and excessive crystal growth.

The particle size and morphology of the LVP/carbon composites were evaluated from TEM images (Fig. 2). The *d*-spacing of the lattice planes of LVP (corresponding to (220), (111), and (-112), respectively) were observed for all the composites, indicating the presence of LVP crystals (Fig. 2d-f). Focusing on the morphology, LVP/KB(5:5) had nano-LVP particles (approximately 50 nm) embedded and well-dispersed in the KB matrix (Fig. 2a) compared to the other composites (Fig. 2a-c). On the other hand, in LVP/KB(7:3) with a low carbon content, nano-LVP particles (approximately 100 nm) were

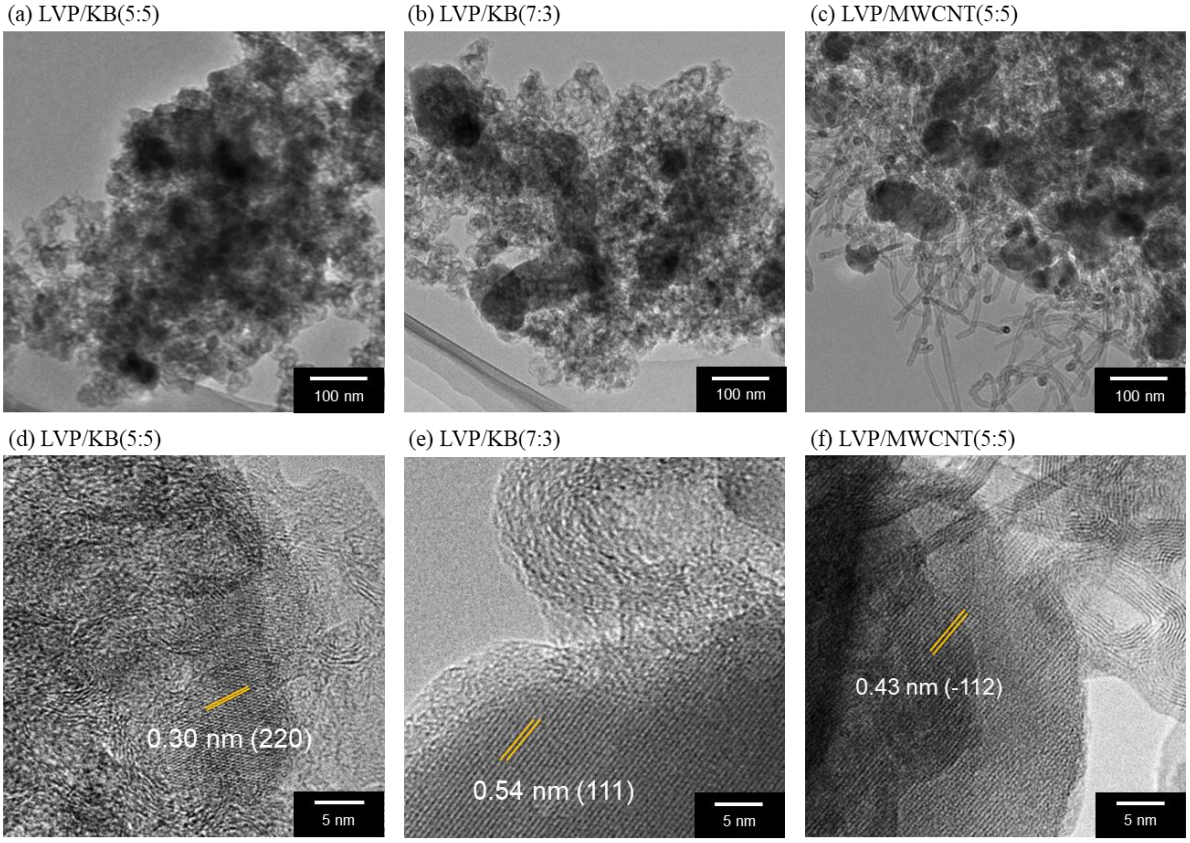


**Figure 2.** High-resolution TEM images of the LVP/carbon composites for (a, d) LVP/KB(5:5), (b, e) LVP/KB(7:3), and (c, f) LVP/MWCNT(5:5). (a-c) Lower-magnification (300,000×) images of the highly dispersed nanosized $Li_3V_2(PO_4)_3$ crystals within the interstices of the carbon (KB or MWCNTs). (d-f) Higher magnification images focusing on representative $Li_3V_2(PO_4)_3$ nanoparticles embedded in the carbon (4,500,000×). Clear lattice fringes with d-spacings of 0.30, 0.54, and 0.43 nm appear, corresponding to the (220), (111), and (−112) planes of $Li_3V_2(PO_4)_3$, respectively.

embedded in the KB (Fig. 2b). For the composite with a different carbon species, LVP/MWCNT (5:5), nano-LVP particles (approximately 100 nm) were observed to be entangled in the MWCNTs (Fig. 2c). Furthermore, compared to LVP/KB(5:5) (Fig. 2d), the boundary between the carbon and LVP particles was more clearly visible for LVP/KB(7:3) and LVP/MWCNT(5:5) (Fig. 2e,f). These XRD, TGA, and TEM results indicate that, LVP/KB(5:5) is characterized by a greater number of junctions between the carbon and LVP precursor, which inhibit excessive crystal growth, thereby resulting in more nanosized LVP particles compared to the other composites.

### Charge–discharge Properties of $V_2(PO_4)_3$/Carbon Composites as a Cathode Material for Magnesium-ion Batteries

Prior to the charge–discharge test of the Mg-ion battery systems, we compared the electrochemical behaviour of the LVP composites using a Li half-cell using the $Li^+$-based electrolyte (1 M $LiPF_6$/EC:DEC) (Fig. S3). The charge–discharge curves of all the composites (Fig. S3a-e) showed three LVP-derived plateaus (Faradaic reaction: 3.6 V, 3.7 V, and 4.1 V *vs.* $Li/Li^+$) [47] and carbon-derived sloping curves (non-Faradaic reaction). For the KB composite systems, the capacity exhibited at 1C-rate increased with increasing carbon content, which could be due to an increase in the carbon-derived exhibited capacity (Fig. S4). Indeed, the electrodes that contained only carbon had capacities of 125 mAh $g^{-1}$ for KB and 20 mAh $g^{-1}$ for the MWCNTs (Fig. S5). After subtraction of the carbon-derived capacities (Fig. S5), the net exhibited capacities of LVP were approximately 100–120 mAh $g^{-1}$ per LVP/KB composites and 120 mAh $g^{-1}$ per the LVP/MWCNT(5:5) composite, which were almost consistent with the theoretical capacities of the LVP (~131.5 mAh $g^{-1}$). All the composites also exhibited high rate characteristics even at 50C-rate, with capacity retention of more than 50% relative to 1C-rate. Thus, the prepared LVP composites functioned properly as ultra-fast Li-ion battery cathodes during $Li^+$ insertion/extraction.

Prior to any charge discharge tests in a $Mg^{2+}$-battery system, $Li^+$ was electrochemically extracted from the LVP/carbon composites to prepare VP/carbon composite cathodes including VP/KB(4:6), VP/KB(5:5), VP/KB(6:4), VP/KB(7:3), and VP/MWCNT(5:5) (see Experimental section). The EELS measurements of delithiated VP/KB(5:5) revealed the absence of a peak corresponding to the K-edge of Li in the range of 60–70 eV, indicating the successful extraction of $Li^+$ from LVP crystals (Fig. S6). Then, the electrochemical $Mg^{2+}$ insertion/extraction behaviour of the VP was investigated using the $Mg^{2+}$-based electrolyte (0.5 M $Mg(TFSA)_2$ + 1 M $SBPBF_4$ / DMC electrolyte).This electrolyte composition was selected to enable a focus on the cathode materials themselves, minimizing the resistance associated with the electrolyte or cathode/electrolyte interface, as demonstrated in a previous report on $FePO_4$[13]. It should be noted that “anode-compatible

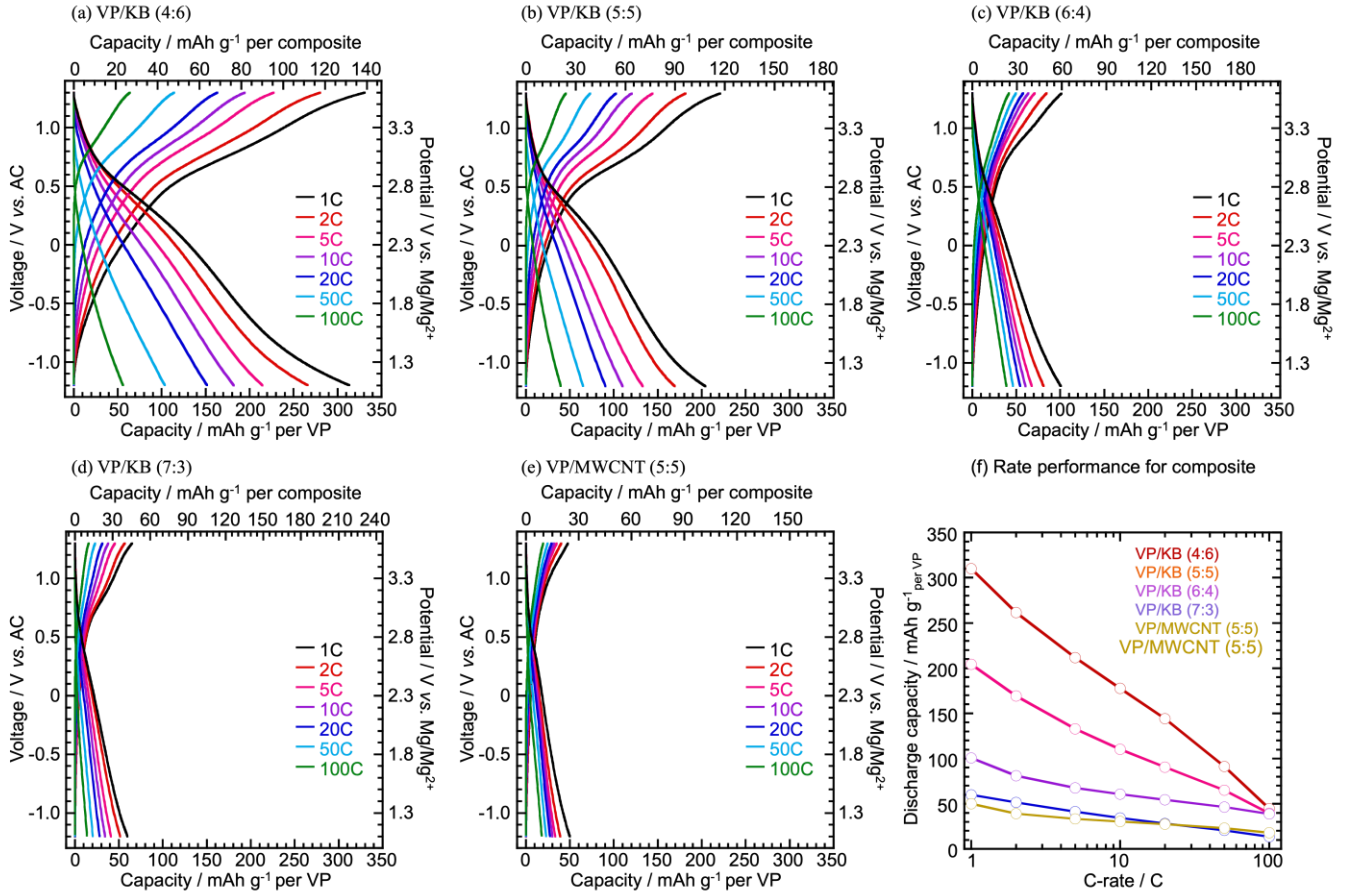


**Figure 3.** (a-e) Charge–discharge plots of (a) VP/KB(4:6), (b) VP/KB(5:5), (c) VP/KB(6:4), (d) VP/KB(7:3) and (e) VP/MWCNT(5:5) using 0.5 M $Mg(TFSA)_2$ + 1 M $SBPBF_4$ / DMC at a rate of 1–100C-rate (1C-rate = 131.5 mAh $g^{-1}$ of $V_2(PO_4)_3$ active material).The charge–discharge voltage range was set at −1.2 to 1.3 V *vs.* AC (corresponding to the potential range of 1.1–3.6 V *vs.* $Mg/Mg^{2+}$) at 1C-rate. (f) Capacity *vs.* C-rate plots of LVP/KB and LVP/MWCNT composites.

electrolytes", such as all-phenyl complex[36], designed for the use with a Mg metal anode, were not applicable due to the high operation potential of VP, which reaches up to 3.6 V vs. $Mg/Mg^+$ and results in the oxidative decomposition of such electrolytes. Charge–discharge curves of VP/KB in $Mg^{2+}$-based electrolyte for initial three cycles are shown in Figure S1. Throughout the initial discharge process, the potential steadily dropped from 0.68 to -1.3 V vs. AC, which corresponds to 3.18 to 1.1 V *vs*. $Mg/Mg^{2+}$, yielding a capacity of 180 mAh $g^{-1}$ per VP. Subsequent two (2nd and 3rd) cycles exhibited nearly identical curves, with minimal irreversible capacity (< 10 mAh $g^{-1}$), indicating the stability and reversibility of the charge-discharge process. The mean charge–discharge potential of VP/KB (2.7 V *vs.* $Mg/Mg^{2+}$) was higher compared with those of the Mg cathode materials previously reported (1.0–2.0 *vs.* $Mg/Mg^{2+}$) as anticipated by DFT.[38] It is also worth noting that the open circuit voltage (OCV) [0.68 V vs. AC] at the 1st discharge process was lower compared to the expected value for the completely charged VP [*ca*. 1.5 V vs. AC]. The reduced potential could be attributed to the partial insertion of $Mg^{2+}$ into VP during the assembly of the VP//AC cell, which is indicative of self-discharge. Fig. 3 shows the rate performance of the VP cathodes with the 0.5 M $Mg(TFSA)_2$ + 1 M $SBPBF_4$ / DMC electrolyte. Focusing on the VP/KB(5:5) cathode (Fig. 3b), the charge–discharge profile exhibited an average reaction potential of approximately 0.4 V *vs.* AC (2.7 V *vs*. $Mg/Mg^{2+}$) at 1C-rate. The shape of the charge–discharge curve was a combination of a single plateau at approximately 0.5 V *vs*. AC (2.8 V *vs.* $Mg/Mg^{2+}$) and a slope over the entire potential range. The former reaction could be derived from the VP redox reaction and the latter from ion absorption/desorption at the KB (discussed later). In addition, from the STEM-EDX results of the VP/KB(5:5) cathode after $Mg^{2+}$-insertion (1.1 V *vs.* $Mg/Mg^{2+}$), the Mg-K edge was observed in the area corresponding to the LVP particles, indicating that $Mg^{2+}$ successfully inserted into the VP particles during discharging (Fig. S7). A comparison of the KB-based composite systems showed that the exhibited capacities per amount of VP material at 1C-rate increased with increasing KB content (VP/KB(4:6): 309 mAh $g^{-1}$, VP/KB(5:5): 204 mAh $g^{-1}$, VP/KB(6:4): 101 mAh $g^{-1}$, and VP/KB(7:3): 60 mAh $g^{-1}$). In addition, the high-KB content systems (VP/KB(4:6) and VP/KB(5:5)) had high exhibited capacities of 200–300 mAh $g^{-1}$ per VP (Fig. 3f), which corresponds to 100–140 mAh $g^{-1}$ per VP/KB composite (Fig. S8), comparable to those of the $Li^+$-based electrolyte systems (200–250 mAh $g^{-1}$ per VP: Fig. S3). Then, we calculated the net VP capacity by subtracting the KB capacity from the VP/KB composite capacity (see Fig. S9). As a result, the VP/KB(4:6) and VP/KB(5:5) systems had high exhibited capacities (100–140 mAh $g^{-1}$ per VP) compared to the low-KB content systems (VP/KB(6:4) and VP/KB(7:3): 10–20 mAh $g^{-1}$ per

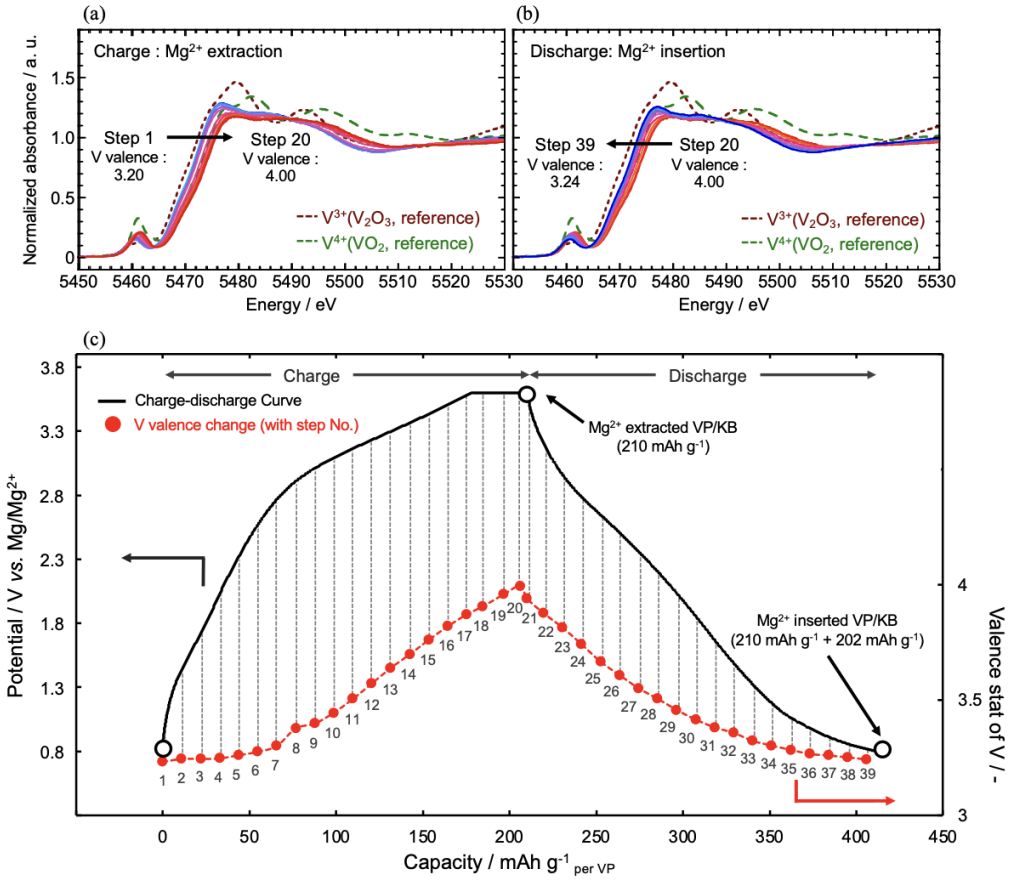


**Figure 4.** (a-b) Normalized V K-edge X-ray absorption near edge structure (XANES) spectra of VP/KB(5:5) during (a) charge ($Mg^{2+}$ extraction) and (b) discharge ($Mg^{2+}$ insertion). Dashed lines represent the reference sample data for $V^{3+}$ ($V_2O_3$, brown line) and $V^{4+}$ ($VO_2$, green line). (c) Charge–discharge profile and valence state of V of VP/KB(5:5) for *in-situ* XAFS measurements at 25°C. The charge–discharge potential range was set at −1.3 to 1.3 V *vs.* AC (corresponding to 1.0–3.6 V *vs.* $Mg/Mg^{2+}$) at 1C-rate. Prior to the XAFS measurements, the cell was discharged under constant-current to –1.3 V *vs.* AC at 0.5C-rate. Note that the valence state of V was calculated by curve fitting using reference sample data for $V^{3+}$ ($V_2O_3$) and $V^{4+}$ ($VO_2$) as shown in Fig. S10.

VP). This result indicates that only VP/KB(4:6) and VP/KB(5:5) are capable of $Mg^{2+}$ insertion/extraction, thus the high-carbon content is an important factor for the activation of the VP for the Mg cathode. In contrast, when the MWCNTs were used as composite carbon (VP/MWCNT, 50 wt%), the capacity per amount of the VP was low (30 mAh $g^{-1}$), indicating that $Mg^{2+}$ insertion/extraction of the VP hardly occurred. Thus, not only high-carbon content but also the species of composite carbon is important for increasing the exhibited capacity of VPs.

The high-rate capabilities of VP/KB (5:5 or 4:6) could be attributed to the nanosizing of VP crystals. Canepa *et al.* predicted that the particle size of the active material and the value of the diffusion barrier may affect the exhibited capacity.[3] In the VP framework, the value of the diffusion barrier is 671 meV for the diffusion of $Mg^{2+}$, thus, to achieve sufficient capacity at 1C-rate, the particle size should be 50 nm or less [49,50]. According to the TEM image (Fig. 2a), VP/KB (5:5) had a smaller particle size (50 nm), which could allow sufficient $Mg^{2+}$ diffusion within the VP at 1C-rate, resulting in a high exhibited capacity (200 mAh $g^{-1}$). On the other hand, VP/MWCNT (5:5) and VP/KB (7:3) had larger particles (approximately 100 nm, Fig. 2b,c), resulting in a poor $Mg^{2+}$ diffusion and lower exhibited capacity (40–50 mAh $g^{-1}$). These results suggest that reducing the size of VP particles to nanometer dimensions can be an effective strategy to ensure a high-rate, and this approach may be also applicable to other reported Mg cathode materials ($FePO_4$, $MgMn_2O_4$ etc.) [25,48]. Further, the exhibited capacity of VP/KB(5:5) was high even at high rates; 170 mAh $g^{-1}$ at 2C-rate, 135 mAh $g^{-1}$ at 5C-rate, and 110 mAh $g^{-1}$ at 10C-rate. Further, we have compiled a summary of reported characteristics data, including exhibited capacity, rate-performance, carbon content, and cyclability, for Mg-ion battery cathode materials operated at room-temperature, along with our VP/KB sample. As shown in Table S2, the VB/KB (5:5) exhibited a relatively high capacity of 100 mAh $g^{-1}$ per composite at 1C-rate compared to other cathode materials at the average potential of 3.3 V *vs.* $Mg/Mg^{2+}$. Since this average potential is one of the highest among tabulated data, the calculated energy density of our KB/VP (5:5) [330 Wh $kg^{-1}$] is compatible to 349 Wh $kg^{-1}$ of $K_2(VO)_2(HPO_4)_2(C_2O_4)\cdot 4.5H_2O$, which has been a benchmark among reported values so far.[49] The following section describes our work to obtain a more in-depth understanding of the $Mg^{2+}$ insertion/extraction mechanism of VP by evaluating the changes in the crystal structure and the valence state of

vanadium. Among the two high-performance cathodes, VP/KB(5:5) and VP/KB(4:6), we selected VP/KB(5:5) because of its relatively low carbon content as this would allow us to more clearly focus on the VP reaction.

**Analysis of $Mg^{2+}$ Insertion/Extraction Mechanism in VP/KB Composite via *in-situ* XAFS and *in-situ* XRD Measurements**

As mentioned in the previous section, VP/KB(5:5) had a high exhibited capacity; however, the detailed reaction potentials and exhibited capacities derived from VP and KB reactions were not fully clarified. The VP/KB reaction could be divided into (1) a Faradaic reaction attributed to the redox reaction of vanadium (which undergoes a valence change) resulting from $Mg^{2+}$ insertion/extraction of VP, and (2) a non-Faradaic reaction (without a valence change of vanadium) by the ion adsorption/desorption on KB. Thus, we conducted *in-situ* XAFS measurements of the V K-edge of VP/KB(5:5) to distinguish between these two reactions (Fig. 4). In the charge–discharge of the *in-situ* XAFS measurement (Fig. 4c), the exhibited capacities (charge: 210 mAh $g^{-1}$, discharge: 202 mAh $g^{-1}$) and the shape of the charge–discharge curve were almost consistent with those of the normal laminate cell (Fig. 3b), thus we judged the charge–discharge process proceeded successfully. The V K-edge X-ray absorption spectra of the VP/KB(5:5) cathode were obtained at various charge–discharge states (Fig. 4a,b), in which the V K-edge absorption edge energy reflected the valence state of the vanadium. For the charging process ($Mg^{2+}$ extraction, Fig. 4a), the absorption edge peak in the V K-edge shifted to lower energy, whereas for the discharging process ($Mg^{2+}$ insertion, Fig. 4b), the absorption edge peak shifted to higher energy. In addition, the intensity of the pre-edge peak (5460 eV), which appears for the high valence states of vanadium ($V^{4+}$ and $V^{5+}$) [50,51] was lower at the initial of charging (step 1, 1.0 V *vs*. $Mg/Mg^{2+}$) and at the end of discharging (step 39, 1.0 V *vs*. $Mg/Mg^{2+}$) than at the end of charging (step 20, 3.6 V *vs*. $Mg/Mg^{2+}$). These results indicate that the vanadium in VP was oxidized during charging ($Mg^{2+}$ extraction) and reduced during discharging ($Mg^{2+}$ insertion).

To quantify the change in valence for vanadium during charge–discharge, the spectra were deconvoluted using $V_2O_3$ and $VO_2$ as the trivalent ($V^{3+}$) and tetravalent ($V^{4+}$) references, respectively. This enabled the valence state of vanadium to be estimated; a typical curve-fitting result is shown in Fig. S10. In the charging process, the initial valence of vanadium (Step 1) was estimated to be +3.2, and this value was estimated to have changed to +4.0 at the end of charging (Step 20). In the case that the valence change of vanadium was only affected by the $Mg^{2+}$ insertion/extraction, the charge reaction could be considered to proceed by the following equation:

$$Mg_{1.3}V_2(PO_4)_3 \rightarrow Mg_{0.5}V_2(PO_4)_3 + 0.8Mg^{2+} + 1.6e^- \quad (1)$$

Assuming the validity of equation (1), the exhibited capacity of VP would be estimated to be 105 mAh $g^{-1}$ during $Mg^{2+}$ extraction. Although the measured charging capacity is higher (210 mAh $g^{-1}$), this value includes the KB-derived exhibited capacity (108 mAh $g^{-1}$, Fig. S9). In fact, subtracting the capacity of KB from the measured charging capacity results in 102 mAh $g^{-1}$, thus the valence change (+0.8) obtained from valence fitting is reasonable. In the discharging process, the vanadium valence states of the initial (Step 20) and final (Step 39) were +4.0 and +3.24, respectively, indicating that the valence of vanadium decreased by 0.76 from the initial state. Considering this valence change, the discharge reaction could be considered to proceed via the following equation:

$$Mg_{0.5}V_2(PO_4)_3 + 0.76Mg^{2+} + 1.52e^- \rightarrow Mg_{1.26}V_2(PO_4)_3 \quad (2)$$

These valence changes of VP are almost the same for the charging (0.8) and discharging (0.76) processes, suggesting that $Mg^{2+}$ insertion/extraction of VP was reversible.

Focusing on the correlation between the valence changes and potential changes, in the charging process, the valence of vanadium hardly changed in the potential range of 1.0–2.5 V *vs*. $Mg/Mg^{2+}$ (Step 1 to Step 5), whereas the valence increased linearly in the range 2.5–3.6 V *vs*. $Mg/Mg^{2+}$ (Step 5 to Step 20). This tendency suggests that in the former region (1.0–2.5 V *vs*. $Mg/Mg^{2+}$), only the KB-derived non-Faradaic reaction contributed to the capacity, whereas in the latter region (2.5–3.6 V *vs*. $Mg/Mg^{2+}$), both the KB-derived non-Faradaic and the VP-derived Faradaic reactions contributed to the capacity. During the discharge process, the valence of vanadium decreased linearly in the 3.6–1.8 V *vs*. $Mg/Mg^{2+}$ (Step 20 to Step 30), whereas the valence of vanadium slightly decreased in the 1.8–1.0 V *vs*. $Mg/Mg^{2+}$ (Step 30 to Step 39). These results indicate that the vanadium was reduced in the high potential region of the charging (2.5 to 3.6 V *vs*. $Mg/Mg^{2+}$) and discharging (3.6 to 1.8 V *vs*. $Mg/Mg^{2+}$) processes. Focusing on the isosbestic point of the XANES profiles (Fig. 4a,b), no clear isosbestic point appeared during $Mg^{2+}$ insertion/extraction of the VP in the potential range of −1.3 to 1.3 V *vs.* AC. In contrast, for $Li_yV_2(PO_4)_3$ ($1 \le y \le 3$), the isosbestic point was observed at 5475 and 5503 eV in this potential range, thus the charge–discharge process via $Li^+$ insertion/extraction of VP was regarded as a two-phase reaction [51,52]. Considering that the no clear isosbestic point was observed, $Mg^{2+}$ insertion/extraction of $V_2(PO_4)_3$ could proceed via a solid-solution (single-phase) reaction rather than by a two-phase reaction.

*In-situ* XRD measurements were performed to clarify the phase transition behavior during $Mg^{2+}$ insertion/extraction of the VP. Fig. 5a shows the *in-situ* XRD profile of VP/KB with the charge ($Mg^{2+}$ extraction) and discharge ($Mg^{2+}$ insertion) curves. The shape of the charge–discharge curves was the same as that of the normal laminate cell (Fig. 3b), indicating that the charge–discharge process was successfully conducted. The peaks observed at the beginning of the charging process (1.1 V *vs.* $Mg/Mg^{2+}$) in the $2\vartheta$ ranges of 20–22°, 27–29°, 29–31°, and 32–35°, respectively, were indexed to monoclinic $V_2(PO_4)_3$ [52]. During the charging process involving $Mg^{2+}$ extraction, none of the peaks in the 1.1–2.5 V *vs.* $Mg/Mg^{2+}$ underwent any changes. This trend indicates that KB mainly contributed to the exhibited capacity in this potential range, which is consistent with the *in-situ* XAFS results (Fig. 4). In the 2.5–3.1 V *vs*. $Mg/Mg^{2+}$, all VP-

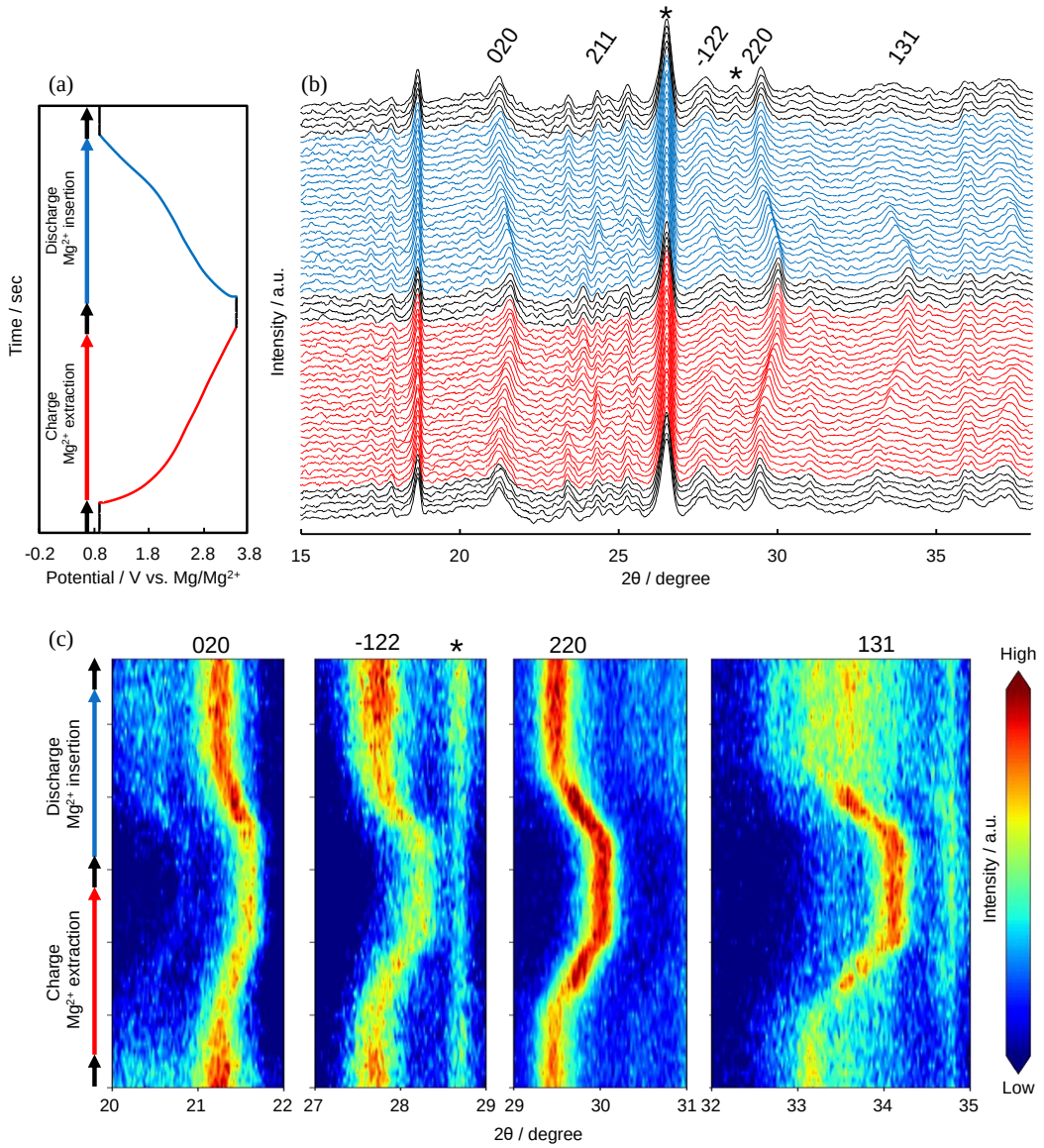


**Figure 5.** (a-c) *In-situ* XRD patterns of VP/KB(5:5): (a) Charge–discharge profile of the VP/KB(5:5) cathode in the *in-situ* XRD cell (see Experimental) using the $Mg^{2+}$-based electrolyte (0.5 M $Mg(TFSA)_2$ + 1 M $SBPBF_4$/DMC) at 25°C. The charge–discharge potential range was set at −1.2 to 1.3 V *vs.* AC (corresponding to 1.1–3.6 V vs. $Mg/Mg^{2+}$) and the charge–discharge rate was 0.25C-rate. (b) *In-situ* XRD patterns during charge–discharge of VP/KB(5:5) in the 15–40° angular range. Asterisks denote reflections from the cell components. (c) Contour plot of *in-situ* XRD patterns in the 20–22°, 27–29°, 29–31°, and 32–35° angular ranges, in which peaks corresponding to the lattice planes of monoclinic $V_2(PO_4)_3$ (JCPDS No. 72-7077) can be observed. All peaks are shifted to higher angles with charging ($Mg^{2+}$ extraction) and to lower angles with discharging ($Mg^{2+}$ insertion). Prior to the XRD measurements, the cell was discharged under constant-current to –1.3 V *vs.* AC at 0.25C-rate.

derived peaks shifted to higher angles (i.e., the unit volume of VP decreased) and no new peaks appeared. Subsequently, in the 3.1–3.6 V *vs*. $Mg/Mg^{2+}$, the peaks corresponding to the (020) and (-122) lattice plane of $V_2(PO_4)_3$ (angular ranges of 20–22°and 27–29°) shifted to higher angles. These *in-situ* XRD results indicate that the $Mg^{2+}$ was extracted from the VP framework by the solid-solution reaction. This particular reaction for the VP is not observed during $Li^+$ insertion/extraction (via a two-phase reaction (Fig. S11)) and could be specific to the $Mg^{2+}$ insertion/extraction, despite the similar range of valence number change; $Mg_xV_2(PO_4)_3$ ($0.5 \le x \le 1.3$: $V^{4+}$-$V^{3.2+}$) and $Li_yV_2(PO_4)_3$ ($1 \le y \le 3$: $V^{4+}$-$V^{3+}$). During the discharge process involving $Mg^{2+}$ insertion, all $V_2(PO_4)_3$-derived peaks shifted to lower angles (i.e., the unit volume of VP increased) in the 3.6–2.3 V *vs*. $Mg/Mg^{2+}$, whereupon no further peak shift was observed below 2.3 V. Thus, the $Mg^{2+}$ insertion/extraction of $V_2(PO_4)_3$ occurred in the same potential range of the charging (2.5 to 3.6 V *vs*. $Mg/Mg^{2+}$) and the discharging (3.6 to 2.3 V *vs*. $Mg/Mg^{2+}$) processes, which are consistent with the *in-situ* XAFS results. These results suggest that the VP framework underwent reversible expansion and shrinkage through the solid-solution reaction during the $Mg^{2+}$ insertion/extraction. This solid-solution reaction was also confirmed by the galvanostatic intermittent titration technique (GITT, Fig. S12). The GITT results revealed different equilibrium potentials for each relaxation step during charge–discharge with a sloping potential change, as is characteristic of solid-solution reactions[26,27].

The solid-solution reaction in the $Mg_xV_2(PO_4)_3$ could be caused by the following two factors: (1) the stoichiometric ratio

of $Mg^{2+}$ entering the $V_2(PO_4)_3$, and (2) strong electrostatic interaction of $Mg^{2+}$ carrier. Focusing on (1), according to the XAFS results of the $Mg_xV_2(PO_4)_3$, the stoichiometric ratio of $Mg^{2+}$ changed from 0.5 to 1.3. This range of $Mg^{2+}$ stoichiometric ratio changes is close to that observed for $Li^+$ in $Li_yV_2(PO_4)_3$ ($0 \le y \le 1$), where the extraction of excess $Li^+$ from LVP leads to a transition from two-phase to solid-solution reaction mechanism.[29,53] This similarity may explain why the phase transition of $Mg_xV_2(PO_4)_3$ proceeds via the solid-solution reaction. Focusing on (2), the charge density of $Mg^{2+}$ is approximately twice as high as that of $Li^+$. Thus, the $Mg^{2+}$–$Mg^{2+}$ electrostatic repulsion and the electrostatic attraction of the $Mg^{2+}$–anion and $Mg^{2+}$–electron are stronger than those in the $Li^+$ system. These interactions lead to slow $Mg^{2+}$ diffusion in the VP framework, which could hinder the process through the quasi-equilibrium route via a two-phase reaction of $Mg_xV_2(PO_4)_3$ [53]. The factors driving the solid-solution reaction in $Mg_xV_2(PO_4)_3$ are still unclear; thus, further research is required to fully understand the phase transition mechanism in detail.

We finally examined the cycle durability of the VP with $Mg^{2+}$ insertion/extraction (Fig. S13). Note that the $Mg^{2+}$ insertion/extraction in LVP through solid-solution reaction within the $Mg^{2+}$ system could potentially result in the collapse of the crystal structure and subsequent degradation. Previous studies have revealed that during $Mg^{2+}$ insertion/extraction of the $FePO_4$ cathode via the solid-solution reaction, the exhibited capacity continuously decreased, accompanied by the collapse of the crystal structure[26,27]. Indeed, with increasing cycles of VP with $Mg^{2+}$ insertion/extraction, the exhibited capacity decreased from 115.1 mAh $g^{-1}$ to 87.5 mAh $g^{-1}$ (after 100 cycles). However, it's worth noting that the corresponding capacity retention of VP/KB (5:5) (76%) is compatible to FP/KB (77%) using same electrolyte composition[37], as tabulated in Table S2. Considering the higher operation potential of VP/KB compared to FP/KB, the obtained result still appears quite promising. Then, after 1,000 cycles, the capacity eventually decreased to 44.7 mAh $g^{-1}$. The electron diffraction in the TEM image of VP revealed that the lattice stripes of spots corresponding to the areal spacing which is observed for the initial state disappeared over 1,000 cycles (Fig. S14). These results indicate that the crystal structure of VP was amorphized during long-term $Mg^{2+}$ insertion/extraction to ultimately result in a low exhibited capacity. To prevent the collapse of the crystal structure and maintain the exhibited capacity, three approaches could be followed in future research: (1) synthesize an amorphous Mg cathode similar to $FePO_4$ [25,54], (2) use the co-insertion of dual carriers ($Mg^{2+}$ and $Li^+$/$Na^+$) to prevent the crystal structure from undergoing drastic changes [42,55], and (3) use a Mg cathode with a low $Mg^{2+}$ diffusion barrier similar to $NaMn_4O_8$ [38].

## Conclusions

Nanocrystalline $V_2(PO_4)_3$ with different carbon contents and species was synthesized by an ultracentrifugation process and characterized as a potential candidate for the cathode in Mg rechargeable batteries. The synthesized $V_2(PO_4)_3$/KB(5:5) composite had nanosized $V_2(PO_4)_3$ particles (50 nm) and showed a high exhibited capacity at 1C-rate (210 mAh $g^{-1}$) and high-rate capability at 10C-rate (110 mAh $g^{-1}$) under ambient conditions (25°C). In addition, the mean reaction potential was approximately 2.7 V *vs*. Mg/$Mg^{2+}$, which is relatively high among those that were previously reported for Mg cathode materials. Thus, the nano-downsized VP is a promising candidate as the cathode for ultrafast and high-energy Mg batteries. *In-situ* XAFS measurements revealed that the $V^3$/$V^{4+}$ redox couple was formed, and the valence of vanadium changed reversibly from +3.2 to +4.0 during the $Mg^{2+}$ insertion/extraction. *In-situ* XRD and GITT results indicated that the phase transition of $Mg_xV_2(PO_4)_3$ ($0.5 \le x \le 1.3$) proceeded via a solid-solution reaction, different from the two-phase reaction for $Li^+$ insertion/extraction of $V_2(PO_4)_3$ in the same potential range (from −1.0 to 1.2 V *vs.* Ag/$Ag^+$). These discoveries should provide the synthesis strategy for the ultrafast cathodes of various multivalent ion batteries and experimental insight into the unique phase transition/valence change behaviour of $V_2(PO_4)_3$ cathodes during $Mg^{2+}$ insertion/extraction.

## Author Contributions

The manuscript was written through contributions of all authors. All authors have given approval to the final version of the manuscript.

## Conflicts of interest

The authors declare no conflict of interest.

## Acknowledgements

This study was supported by JSPS KAKENHI (Grant Nos. JP19H00882, JP20H02823, JP21K14711, JP21K05241, and JP22K14759), and the Center of Innovation Program from Japan Science and Technology Agency (A-STEP; AS282S002d). The synchrotron radiation experiments were performed at SPring-8 with the approval of the Japan Synchrotron Radiation Research Institute (JASRI) (Proposal no. 2021A1356).

## References`

1 P. Greim, A. A. Solomon and C. Breyer, *Nat. Commun.*, 2020, **11**, 4570.

2 Y. Tian, G. Zeng, A. Rutt, T. Shi, H. Kim, J. Wang, J. Koettgen, Y. Sun, B. Ouyang, T. Chen, Z. Lun, Z. Rong, K. Persson and G. Ceder, *Chem. Rev.*, 2021, **121**, 1623–1669.

3 P. Canepa, G. Sai Gautam, D. C. Hannah, R. Malik, M. Liu, K. G. Gallagher, K. A. Persson and G. Ceder, *Chem. Rev.*, 2017, **117**, 4287–4341.

4 F. Liu, T. Wang, X. Liu and L.-Z. Fan, *Adv. Energy Mater.*, 2021, **11**, 2000787.

5 Y. Orikasa, T. Masese, Y. Koyama, T. Mori, M. Hattori, K. Yamamoto, T. Okado, Z.-D. Huang, T. Minato, C. Tassel, J. Kim, Y. Kobayashi, T. Abe, H. Kageyama and Y. Uchimoto, *Sci. Rep.*, 2014, **4**, 5622.

6 B. Mason, *Principles of geochemistry*, John Wiley & Sons, Nashville, TN, 4th edn., 1982.
7 M. Matsui, *J. Power Sources*, 2011, **196**, 7048–7055.
8 D. Aurbach, Z. Lu, A. Schechter, Y. Gofer, H. Gizbar, R. Turgeman, Y. Cohen, M. Moshkovich and E. Levi, *Nature*, 2000, **407**, 724–727.
9 Y. A. Wu, Z. Yin, M. Farmand, Y.-S. Yu, D. A. Shapiro, H.-G. Liao, W.-I. Liang, Y.-H. Chu and H. Zheng, *Sci. Rep.*, 2017, **7**, 42527.
10 S. H. Lapidus, N. N. Rajput, X. Qu, K. W. Chapman, K. A. Persson and P. J. Chupas, *Phys. Chem. Chem. Phys.*, 2014, **16**, 21941–21945.
11 R. Mohtadi and F. Mizuno, *Beilstein J. Nanotechnol.*, 2014, **5**, 1291–1311.
12 R. Attias, M. Salama, B. Hirsch, Y. Gofer and D. Aurbach, *ChemElectroChem*, 2018, **5**, 3514–3524.
13 Z. Q. Rong, R. Malik, P. Canepa, G. S. Gautam, M. Liu, A. Jain, K. Persson and G. Ceder, *Chem. Mater.*, 2015, **27**, 6016–6021.
14 G. Gershinsky, H. D. Yoo, Y. Gofer and D. Aurbach, *Langmuir*, 2013, **29**, 10964–10972.
15 K. W. Nam, S. Kim, S. Lee, M. Salama, I. Shterenberg, Y. Gofer, J.-S. Kim, E. Yang, C. S. Park, J.-S. Kim, S.-S. Lee, W.-S. Chang, S.-G. Doo, Y. N. Jo, Y. Jung, D. Aurbach and J. W. Choi, *Nano Lett.*, 2015, **15**, 4071–4079.
16 S.-B. Son, T. Gao, S. P. Harvey, K. X. Steirer, A. Stokes, A. Norman, C. Wang, A. Cresce, K. Xu and C. Ban, *Nat. Chem.*, 2018, **10**, 532–539.
17 A. Emly and A. Van der Ven, *Inorg. Chem.*, 2015, **54**, 4394–4402.
18 X. Sun, P. Bonnick, V. Duffort, M. Liu, Z. Rong, K. A. Persson, G. Ceder and L. F. Nazar, *Energy Environ. Sci.*, 2016, **9**, 2273–2277.
19 X. Sun, P. Bonnick and L. F. Nazar, *ACS Energy Lett.*, 2016, **1**, 297–301.
20 B. Liu, T. Luo, G. Mu, X. Wang, D. Chen and G. Shen, *ACS Nano*, 2013, **7**, 8051–8058.
21 K. Kajihara, D. Takahashi, H. Kobayashi, T. Mandai, H. Imai and K. Kanamura, *RSC Adv.*, 2021, **11**, 19076–19082.
22 H. Kobayashi, K. Samukawa, M. Nakayama, T. Mandai and I. Honma, *ACS Appl. Nano Mater.*, 2021, **4**, 8328–8333.
23 H. Kobayashi, Y. Fukumi, H. Watanabe, R. Iimura, N. Nishimura, T. Mandai, Y. Tominaga, M. Nakayama, T. Ichitsubo, I. Honma and H. Imai, *ACS Nano*, 2023, **17**, 3135-3142.
24 Z.-D. Huang, T. Masese, Y. Orikasa, T. Mori and K. Yamamoto, *RSC Adv.*, 2015, **5**, 8598–8603.
25 Y. Orikasa, K. Kisu, E. Iwama, W. Naoi, Y. Yamaguchi, Y. Yamaguchi, N. Okita, K. Ohara, T. Munesada, M. Hattori, K. Yamamoto, P. Rozier, P. Simon and K. Naoi, *Chem. Mater.*, 2020, **32**, 1011–1021.
26 A. Watanabe, K. Yamamoto, Y. Orikasa, T. Masese, T. Mori, T. Uchiyama, T. Matsunaga and Y. Uchimoto, *Solid State Ionics*, 2020, **349**, 115311.
27 R. Zhang and C. Ling, *ACS Appl. Mater. Interfaces*, 2016, **8**, 18018–18026.
28 C. Ling, D. Banerjee, W. Song, M. Zhang and M. Matsui, *J. Mater. Chem.*, 2012, **22**, 13517–13523.
29 S.-C. Yin, H. Grondey, P. Strobel, M. Anne and L. F. Nazar, *J. Am. Chem. Soc.*, 2003, **125**, 10402–10411.
30 Y. Orikasa, T. Maeda, Y. Koyama, H. Murayama, K. Fukuda, H. Tanida, H. Arai, E. Matsubara, Y. Uchimoto and Z. Ogumi, *Chem. Mater.*, 2013, **25**, 1032–1039.
31 R. Malik, A. Abdellahi and G. Ceder, *J. Electrochem. Soc.*, 2013, **160**, A3179.
32 K. Naoi, K. Kisu, E. Iwama, Y. Sato, M. Shinoda, N. Okita and W. Naoi, *J. Electrochem. Soc.*, 2015, **162**, A827.
33 K. Naoi, K. Kisu, E. Iwama, S. Nakashima, Y. Sakai, Y. Orikasa, P. Leone, N. Dupré, T. Brousse, P. Rozier, W. Naoi and P. Simon, *Energy Environ. Sci.*, 2016, **9**, 2143–2151.
34 M. Y. Saıdi, J. Barker, H. Huang, J. L. Swoyer and G. Adamson, *Electrochem. Solid-State Lett.*, 2002, **5**, A149.
35 A. Yamada, S. C. Chung and K. Hinokuma, *J. Electrochem. Soc.*, 2001, **148**, A224.
36 H. Huang, S.-C. Yin, T. Kerr, N. Taylor and L. F. Nazar, *Adv. Mater.*, 2002, **14**, 1525–1528.
37 Y. Chikaoka, N. Nakata, K. Fujii, S. Sawayama, R. Ochi, E. Iwama, N. Okita, Y. Harada, Y. Orikasa, W. Naoi and K. Naoi, *ACS Appl. Energy Mater.*, 2023, **6**, 4657–4670.
38 A. Rutt, J.-X. Shen, M. Horton, J. Kim, J. Lin and K. A. Persson, *ACS Appl. Mater. Interfaces*, 2022, **14**, 44367–44376.
39 S.-C. Yin, P. S. Strobel, H. Grondey and L. F. Nazar, *Chem. Mater.*, 2004, **16**, 1456–1465.
40 A. Tang, X. Wang, G. Xu, R. Peng and H. Nie, *Mater. Lett.*, 2009, **63**, 2396–2398.
41 M. Onoda and H. Hirose, *J. Phys. Soc. Jpn.*, 2012, **81**, 094801.
42 C. Li, W. Wu, Y. Liu, X. Yang, Z. Qin, Z. Jia and X. Sun, *J. Power Sources*, 2022, **520**, 230853.
43 E. Iwama, N. Kawabata, N. Nishio, K. Kisu, J. Miyamoto, W. Naoi, P. Rozier, P. Simon and K. Naoi, *ACS Nano*, 2016, **10**, 5398–5404.
44 E. Iwama, P. Simon and K. Naoi, *Current Opinion in Electrochemistry*, 2017, **6**, 120–126.
45 D. Morgan, G. Ceder, Saïdi, J. Barker, J. Swoyer, H. Huang and G. Adamson, *Chem. Mater.*, 2002, **14**, 4684–4693.
46 B. E. Warren, *X-ray Diffraction*, Courier Corporation, 1990.
47 A. L. Lipson, S.-D. Han, B. Pan, K. A. See, A. A. Gewirth, C. Liao, J. T. Vaughey and B. J. Ingram, *J. Electrochem. Soc.*, 2016, **163**, A2253.
48 R. Yokozaki, H. Kobayashi and I. Honma, *Ceram. Int.*, 2021, **47**, 10236–10241.
49 C. Li, L. Lin, W. Wu and X. Sun, *Small Methods*, 2022, **6**, e2200363.
50 J. Yoon, S. Muhammad, D. Jang, N. Sivakumar, J. Kim, W.-H. Jang, Y.-S. Lee, Y.-U. Park, K. Kang and W.-S. Yoon, *J. Alloys Compd.*, 2013, **569**, 76–81.
51 T. Ruan, S. Lu, J. Lu, J. Niu and R. Li, *Energy Storage Materials*, 2023, **55**, 546–555.
52 S. Kim, Z. Zhang, S. Wang, L. Yang, E. J. Cairns, J. E. Penner-Hahn and A. Deb, *J. Phys. Chem. C*, 2016, **120**, 7005–7012.
53 H. Huo, Z. Lin, G. Zhong, S. Lou, J. Wang, Y. Ma, C. Dai, Y. Xiong, G. Yin and Y. Yang, *J. Mater. Chem. A Mater. Energy Sustain.*, 2022, **67**, 593–603.

54 V. Mathew, S. Kim, J. Kang, J. Gim, J. Song, J. P. Baboo, W. Park, D. Ahn, J. Han, L. Gu, Y. Wang, Y.-S. Hu, Y.-K. Sun and J. Kim, *NPG Asia Materials*, 2014, **6**, e138–e138.

55 M. Rashad, H. Zhang, X. Li and H. Zhang, *J. Mater. Chem. A Mater. Energy Sustain.*, 2019, **7**, 9968–9976.